

Article

Enhancement of Optical Activity and Properties of Barium Titanium Oxides to Be Active in Sunlight through Using Hollandite Phase Instead of Perovskite Phase

Adil Alshoaibi ^{1,*}, Osama Saber ^{1,2} and Faheem Ahmed ¹

¹ Department of Physics, College of Science, King Faisal University, P.O. Box 400, Al-Ahsa 31982, Saudi Arabia; osmohamed@kfu.edu.sa (O.S.); fahmed@kfu.edu.sa (F.A.)

² Egyptian Petroleum Research Institute, Nasr City, P.O. Box 11727, Cairo 11765, Egypt

* Correspondence: adshoaibi@kfu.edu.sa; Tel./Fax: +966-013589-9417

Abstract: The present study aims to enhance the optical properties of barium titanate through narrowing its band gap energy to be effective for photocatalytic reactions in sunlight and be useful for solar cells. This target was achieved through growth of the hollandite phase instead of the perovskite phase inside the barium titanate crystals. By using solvent thermal reactions and thermal treatment at different temperatures (250 °C, 600 °C, and 900 °C), the hollandite phase of barium titanate was successfully obtained and confirmed through X-ray diffraction (XRD), Raman spectra and scanning electron microscopy techniques. XRD patterns showed a clear hollandite phase of barium titanium oxides for the sample calcined at 900 °C (BT1-900); however, the samples at 600 °C showed the presence of mixed phases. The mean crystallite size of the BT1-900 sample was found to be 38 nm. Morphological images revealed that the hollandite phase of barium titanate consisted of a mixed morphology of spheres and sheet-like features. The optical properties of barium titanate showed that its absorption edge shifted to the visible region and indicated band gap energy tuning ranging from 1.75 eV to 2.3 eV. Photocatalytic studies showed the complete and fast decolorization and mineralization of green pollutants (naphthol green B; NGB) in the prepared barium titanate with hollandite phase after illumination in sunlight for ten minutes. Finally, it can be concluded that the low band gap energy of barium titanate having the hollandite phase introduces beneficial structures for optical applications in sunlight.

Keywords: low band gap energy; hollandite structure; barium titanate; optical properties; photocatalytic degradation



Citation: Alshoaibi, A.; Saber, O.; Ahmed, F. Enhancement of Optical Activity and Properties of Barium Titanium Oxides to Be Active in Sunlight through Using Hollandite Phase Instead of Perovskite Phase. *Crystals* **2021**, *11*, 550. <https://doi.org/10.3390/cryst11050550>

Academic Editors: Alexander S. Novikov and Assem Barakat

Received: 2 April 2021

Accepted: 8 May 2021

Published: 15 May 2021

Publisher's Note: MDPI stays neutral with regard to jurisdictional claims in published maps and institutional affiliations.



Copyright: © 2021 by the authors. Licensee MDPI, Basel, Switzerland. This article is an open access article distributed under the terms and conditions of the Creative Commons Attribution (CC BY) license (<https://creativecommons.org/licenses/by/4.0/>).

1. Introduction

In order to remove pollutants at low concentrations, as well as for the removal of harmful chemicals, photocatalysis has attracted great attention as an effective method [1,2]. Titanium dioxide (TiO₂) has attracted great attention as a photocatalyst [1–8] because of its strong oxidative power activated under the illumination of ultraviolet (UV) [4,5] or visible light [6–8]. However, to deal with a variety of harmful chemicals under different conditions, a diverse range of photocatalysts is needed, which could resolve the problems. Among the oxides, perovskite-type materials possess photostability and outstanding photocatalytic activity. This outstanding property results from the unique structures with larger lattice distortion and defects by trapping holes, thus preventing the formation of electron-hole pairs [9–11]. Additionally, stimulation of the adsorption of oxygen on the surface of cations, due to the vacancy of metal in the perovskite-type structure, resulted in enhancing the photocatalytic reaction [11].

In particular, BaTiO₃ is a typical perovskite photocatalyst with unique physical and chemical properties, which could be governed by its surface morphology and particle size; hence, nanostructured materials with high purity are greatly needed [12]. By changing

the chemical composition or performing thermal treatment of these ceramics, the physical properties of these ceramics change drastically, and they transform to other forms such as barium hollandites or titanate hollandites.

Hollandites can be defined by using unit-cell formula $A_xB_8O_{16}$, where A denotes ions in the tunnel cavities of the structure (e.g., Ba, Cs), while B represents smaller cations including Al^{3+} , Ga^{3+} , Cr^{3+} and Ti^{4+} , which reside in octahedral sites. Tetragonal (space group I4/m) or monoclinic (C2/m) structures could be assigned to the hollandites [13,14].

More specifically, titanate hollandites, which have the compositions $A_x(Ti^{4+}, B)_8O_{16}$ (where A = Ba^{2+} , Cs^+ , Sr^{2+} , Rb^+ , etc.; B = Al^{3+} , Fe^{3+} , Mg^{2+} , Ti^{3+} , Ga^{3+} , Cr^{3+} , Sc^{3+} , etc.) [15–21], are structural analogs of the prototype hollandite, $Ba(Mn^{4+}, Mn^{3+})_8O_{16}$ [22]. In the structure, $[TiO_6]$ and $[BO_6]$ octahedral are linked via edge- and corner-sharing to form a three-dimensional framework, in which Ti^{4+} and B^{3+} are disordered over one or two crystallographically distinct sites. A^+ or A^{2+} cations occupy the box-shaped cavity sites, each coordinated by eight oxygen atoms, within tunnels parallel to the c-axis. The adoption of either a tetragonal (space group I4/m) or monoclinic (space group I2/m) symmetry usually depends on the ratio of mean radius of cations in the A and Ti/B sites [15,21]. The catalytic properties of thermally activated hollandite compounds have been investigated and reported previously [23–25]. In addition, the photocatalytic properties on the hollandites by selective decomposition of nitric oxide in the gas phase and nitrate ions in water have also been examined [26–29]. These observations suggested that hollandites might prove to be promising photocatalysts.

In this study, the enhancement in the optical properties of barium titanium oxides with hollandite phase, in order to make them active in visible light for the utilization of the hollandite-type compound as an efficient photocatalyst, is reported.

2. Experimental Details

Barium carbonate (99.9%), titanium(IV) isopropoxide (97%) and zinc acetate dehydrate (98%) were acquired from Sigma Aldrich. Barium carbonate (7 g) was reacted with 10 mL HCL (37%) and 20 mL water. Titanium isopropoxide (10.3 g) was reacted with 180 mL ethanol. The two solutions were mixed together inside an autoclave. An appropriate amount of water was used for forming a milky solution. An excess amount of methanol (350 mL) was added to the milky solution. A closed and pressurized vessel (autoclave) was used for keeping the mixture at a temperature = 250 °C and under high pressure (10 bar) for 2 h. After 2 h, the system was shut down and the pressure was released with an inert gas (Argon). The product was called BT1. By adding zinc acetate (0.08 g) as a dopant for the above solution, another nanocomposite was prepared by the same technique. This product was coded as BT2. These two different crystalline nanostructures of barium titanium oxides, BT1 and BT2, were prepared by using a high pressure of alcohol. By thermal treatment of these two samples at 600 °C and 900 °C, four types of crystalline nanostructures were produced and coded as BT1-600, BT1-900, BT2-600 and BT2-900, respectively. Commercial nanoparticles of barium titanium oxide were used for the comparison.

To characterize the prepared samples, the powder X-ray diffraction technique was used for detecting the crystalline structure and the different phases of barium titanate by Bruker-AXS, Karlsruhe, Germany with Cu-K radiation ($\lambda = 0.154$ nm). The morphology and size of the synthesized product were measured by field emission scanning electron microscopy (FESEM) using a JEOL electron microscope (JSM-7500, Akishima, Tokyo, Japan). HORIBA Jobin Yvon Lab RAM HR was used for determining the Raman spectrum of the prepared samples. The excitation for the prepared samples depended on the source of a 633 nm laser. For measuring the optical properties of the prepared materials, a UV/VIS/NIR Shimadzu 3600 spectrophotometer with an attached integrating sphere (ISR-603) (Shimadzu, Columbia, MD, USA) was used to determine the diffuse reflectance of the solid materials.

Photocatalytic degradation reactions of naphthol green B (NGB) in sunlight were used to determine the photoactivity of the prepared materials. In the current study, the prepared

aqueous solution of NGB (4×10^{-4} M) was mixed with 0.1 g of the prepared material and illuminated in sunlight through a 10 cm^2 radiation area. Depending on the intensity of the measured spectrum of the dye, the concentration of the dye was determined according to the law of Beer-Lambert. The absorbance of the samples was measured after ten minutes of sunlight irradiation using the UV-Vis spectrophotometer. By following the integrated area of the characteristic peak of NGB at 714 nm, the decomposition of the green dyes was calculated. The photocatalytic experiments of NGB were carried out during the summer season (July) in Saudi Arabia under irradiation by sunlight in the period of 9:30 A.M. and 10:30 A.M.

3. Results and Discussion

X-ray diffraction (XRD) was used to characterize the crystalline structures and chemical formulae of the prepared barium titanium oxides. The XRD patterns of BT1 are shown in Figure 1. It shows clear peaks for BT1-900 at $2\theta = 17.65, 25.14, 27.94, 31.58, 36.36, 39.90, 40.52, 48.20, 54.66, 58.21$ and 67.135° , which are in accordance with the hollandite phase of barium titanium oxides with chemical formulae $\text{Ba}_{1.12}(\text{Ti}_8\text{O}_{16})$, as shown in JCPDS file No. 77-0883. Figure 1 shows that the peaks of BT1-900 are indexed to the diffraction planes of hollandite phase [200], [220], [130], [101], [121], [240], [301], [411], [600], [251] and [541].

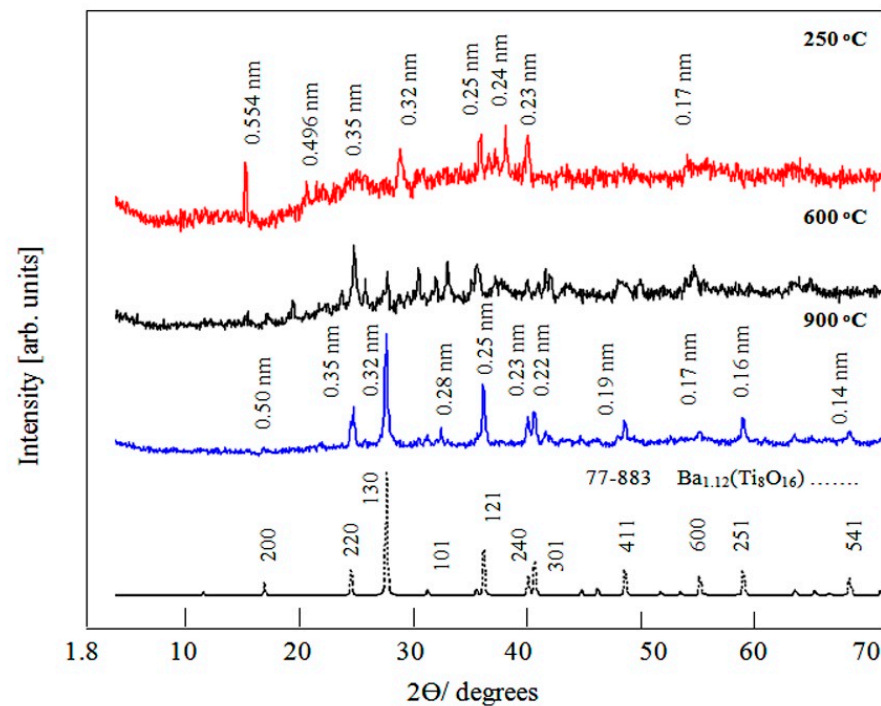


Figure 1. XRD patterns of BT1 at different temperatures.

The basic formula of hollandite is AB_8O_{16} , with the A-site often occupied by larger mono-and/or divalent cations and the B-site by smaller tri-and/or tetravalent cations. The formation of the hollandite phase resulted from a framework composed of BO_6 octahedra with tunnels along the C-axis in which the larger A-cations are located. Due to the barium deficiency in the stoichiometry, barium titanium hollandite is formed. The symmetry of the crystal structure of $\text{Ba}_{1.12}(\text{Ti}_8\text{O}_{16})$ can be tetragonal. Therefore, the crystal structure consists of octahedra of TiO_6 , and partially occupied Ba-cations on the tunnel sites. Barium hollandites may exhibit long-range ordering of barium cations and vacancies in the tunnels and have the possibility to be commensurate [30].

In addition, the diffraction peaks with remarkable broadening revealed the crystallinity in the nanoscale regime of the sample of BT1-900 particles. Therefore, the crystalline size was calculated using the Debye–Scherrer formula:

$$D = k\lambda / \beta \cos\theta$$

where k is constant (shape factor around 0.9), λ corresponds to the wavelength of the X-ray used (1.5418×10^{-10} m), β is the FWHM of the diffraction line, and θ is the angle of the diffraction. The mean crystallite size of the BT1-900 particles measured from XRD peaks with widths of [220], [130] and [411] was calculated to be 38 nm.

However, the samples BT1 and BT1-600 showed mixed phases. The XRD patterns of the sample BT1 show the peak at $2\theta = 15.98^\circ$, indicating the reflection of plane [111] of barium hydroxide, as shown in JCPDS file No. 26-0155. In addition, it shows a clear peak at $2\theta = 38.13^\circ$, indicating the presence of the rutile phase of titanium oxide, in accordance with JCPDS file No. 75-1753. The other peaks are weak and due to barium titanium oxides. The sample BT1-600 showed the disappearance of the peak of barium hydroxide and appearance of a clear peak at $2\theta = 25.14^\circ$, indicating the presence of anatase phase of titanium oxide, in accordance with JCPDS file No. 84-1286. The other peaks are due to the barium titanium oxide. According to these XRD data, the thermal treatment at 900°C is considered necessary to obtain the pure phase of barium titanium oxides $\text{Ba}_{1.12}(\text{Ti}_8\text{O}_{16})$.

In the case of BT2, the XRD patterns showed that BT2-900 consists of two phases of barium titanium oxides: perovskite phase BaTiO_3 and hollandite $\text{Ba}_{1.12}(\text{Ti}_8\text{O}_{16})$. Figure 2 shows two series of peaks for BT2-900. The first series revealed the peaks at $2\theta = 17.86, 20.14, 23.99, 26.38, 28.57, 35.33, 40.0, 49.05, 54.25$ and 59.24 . These peaks were well matched with the standard diffraction planes of $\text{Ba}_{1.12}(\text{Ti}_8\text{O}_{16})$ phase as shown in JCPDS file No. 77-0883. The second series showed peaks at $2\theta = 22.33, 31.58, 38.86, 45.1, 56.22$ and 66.1 . These peaks were in accordance with the standard entire diffraction planes of the BaTiO_3 phase, as shown in JCPDS file No. 74-1964. By analyzing the main peak of both phases, the mean crystallite sizes of both BaTiO_3 and $\text{Ba}_{1.12}(\text{Ti}_8\text{O}_{16})$ were estimated by the Debye–Scherer equation. The particle sizes of BaTiO_3 and $\text{Ba}_{1.12}(\text{Ti}_8\text{O}_{16})$ were 44 nm and 47 nm, respectively. The samples BT2 and BT2-600, which were thermally treated at a lower temperature, showed only one phase of barium titanium oxide, BaTiO_3 , mixed with the crystalline phase of barium chloride, as shown in JCPDS file No. 25-1135 and in Figure 2.

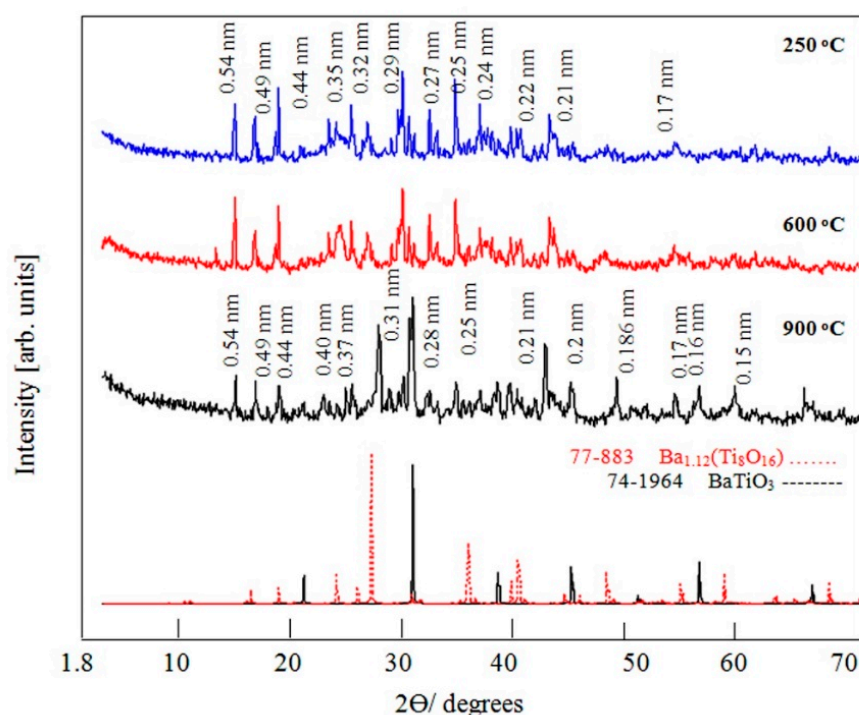


Figure 2. XRD patterns of BT2 at different temperatures.

Although, zinc acetate has been used as a dopant in the BT2 samples, there are no peaks observed in the X-ray pattern, which indicates that zinc is homogeneously dispersed inside the structure. In addition, it has a positive role in growing the perovskite phase, in accordance with the results of Gao et al., which indicated the role of zinc dopants for the crystallization of BaTiO₃ perovskite [31].

The microstructural studies of the hollandite titanate were performed by FESEM. The morphological features of the BT1 sample are depicted in Figure 3. In Figure 3a, micrographs of the as-prepared sample reveal a dense microstructure, composed of spherical particles of micron size. With an increase in temperature to 600 °C, Figure 3b depicts that the well-defined sphere shape, with a smooth surface and clear grain boundary, was observed. These clear spheres showed that a good crystalline phase was observed at this temperature. With a further increase in temperature to 900 °C, a mixed morphology of spheres and sheet-like features was observed (Figure 3c).

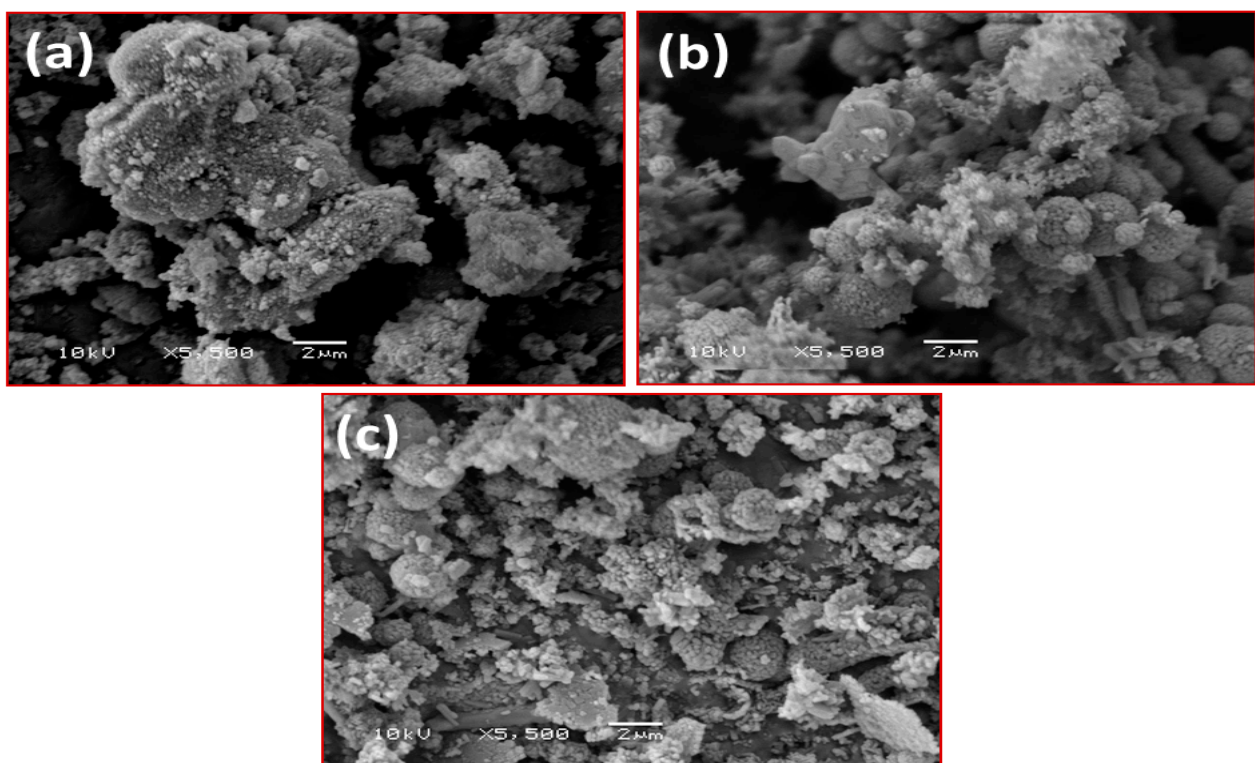


Figure 3. FESEM images of BT1 samples: (a) as-prepared, (b) calcined at 600 °C, (c) calcined at 900 °C. Scale bar in (a–c) is 2 μm.

Figure 4 depicts the morphology of the BT2 samples calcined at different temperatures. It is clear from Figure 4a that as-prepared samples produced a dense, spherical particle-like morphology similar to that of the BT1 samples with smaller-sized particles. With the increase in temperature, BT2 samples at 600 °C (Figure 4b) showed improved crystalline features of spherical particles assembled in a sphere and distributed all over the surface with high density. BT2 samples calcined at 900 °C, as shown in Figure 4c, consisted of a very clear sphere with excellent crystallinity having small spheres attached to their surfaces, which makes them unique. The morphological studies revealed that by increasing the temperature, the morphology of hollandite titanate was changed, with improved crystal quality.

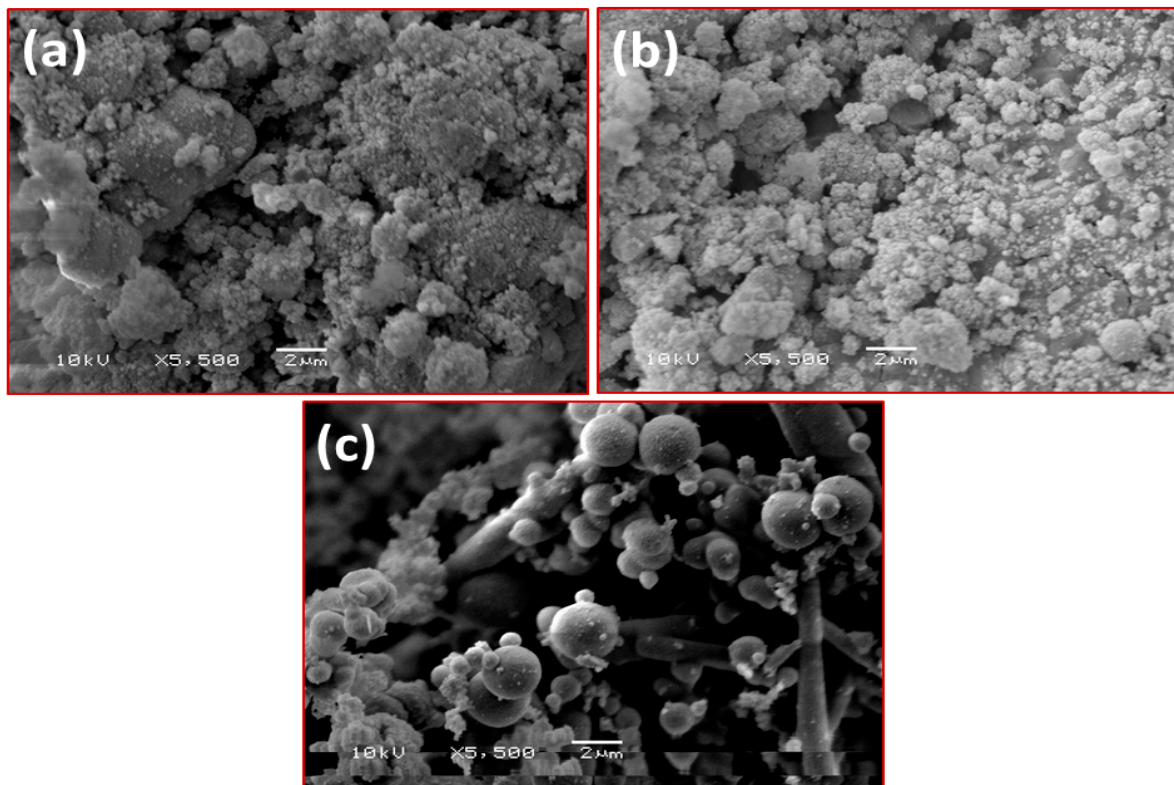


Figure 4. FESEM images of BT2 samples: (a) as-prepared, (b) calcined at 600 °C, (c) calcined at 900 °C. Scale bar in (a–c) is 2 μm.

Figure 5 shows the Raman spectra of BT1 samples calcined at different temperatures, while Figure 6 shows Raman spectra of BT2 samples. It could be clearly seen from the Raman spectra of BT1 and BT2 samples that Raman active vibration modes were observed in the frequency range 100–800 cm^{-1} , which are in close agreement with the compounds of the hollandite type [32].

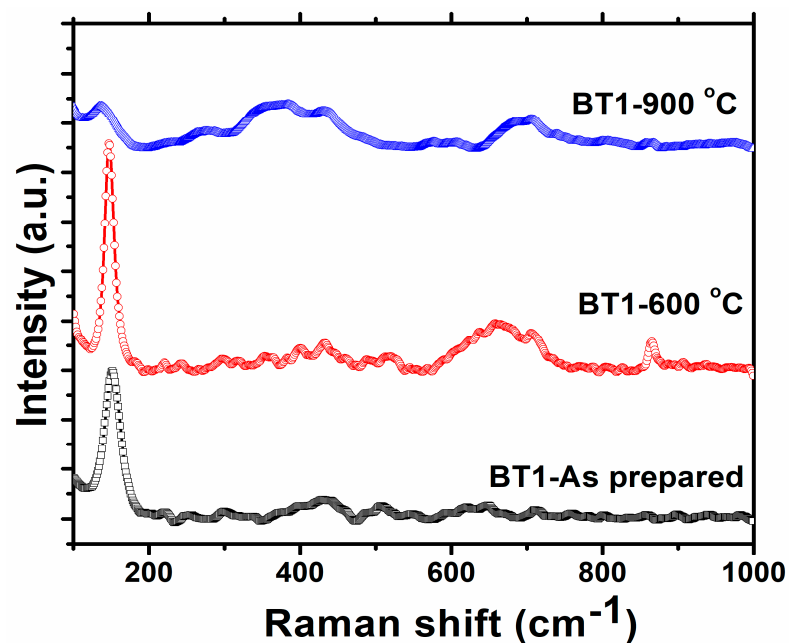


Figure 5. Raman spectra of BT1 sample calcined at different temperatures.

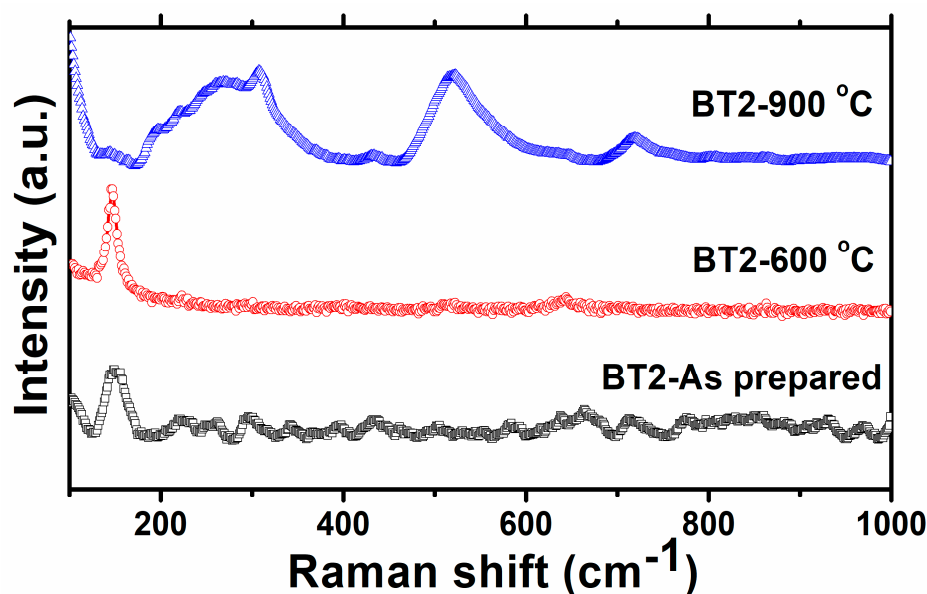


Figure 6. Raman spectra of BT2 sample calcined at different temperatures.

For as-prepared BT1 samples, as shown in Figure 5, there are Raman peaks that appear at 152.6, 432.7, 511.3, 656.8 and 711.1 cm^{-1} . The Raman spectrum of BT1 samples calcined at 600 $^{\circ}\text{C}$ showed modifications in the peaks which are positioned at 147.0, 432.1, 519.5, 663.0 and 705.2 cm^{-1} . With the further increase in temperature to 900 $^{\circ}\text{C}$, the BT1-900 sample showed peaks positioned at 137.0, 365.5, 436.3, 588.3 and 705.2 cm^{-1} . The band near 136–152 cm^{-1} was assigned to the B_{1g} mode, which occurs due to the rotational vibration of oxygen atoms in TiO₆ octahedra [33–35]. It was noted that with an increase in the calcination temperature to 900 $^{\circ}\text{C}$, this band shifted towards a lower wavenumber with a change in intensity. The band positioned near 432 cm^{-1} is assigned to the E_g mode, which resulted from the symmetric stretching vibration of the Ti–O bond [36,37].

The peaks near 365, 511, 663 and 705 cm^{-1} might correspond to the bending mode of TiO₆ octahedra [38–40]. One can see that a shift and the appearance of some peaks in the Raman spectra of BT1 samples with increasing temperature were observed, which implies that the hollandite system undergoes a structural transition. In the Raman spectra of BT2 samples calcined at different temperatures, as shown in Figure 6, as-prepared samples showed peaks appearing at 150.90, 298, 434.90 and 665.81 cm^{-1} . With the increase in temperature to 600 $^{\circ}\text{C}$, BT2 samples showed only two peaks near 147.09 and 643.09 cm^{-1} . With a further increase in temperature to 900 $^{\circ}\text{C}$, the Raman spectra of BT2 samples consisted of peaks positioned at 141.45, 268.18, 306, 432.90, 520 and 720 cm^{-1} .

It is clear that there are various changes in the Raman spectra that indicated the phase transition as temperature increased. The modification in the intensity and position of the band, ranging from 136 to 152 cm^{-1} , with the increase in temperature, resulted from the changes in the TiO₆ octahedra in the symmetric stretching modes [40]. It was observed that by the phase transition, TiO₆ octahedra's bending mode was also affected, which could be explained by the observed changes in the intensity of the band and peak positions near 300, 520 and 720 cm^{-1} . The appearance of some peaks, such as at 665 cm^{-1} , and their extinction with increasing temperature, indicated the phase transition with the temperature [40].

The effect of the hollandite phase of Ba_{1.12}(Ti₈O₁₆) on the optical properties of the perovskite phase of barium titanium oxides was studied by UV–Vis absorption. Figure 7 shows the UV–Vis absorption spectra for the pure phase of BaTiO₃, BT1-900 and BT2-900. The strong increase in absorbance, which was observed as cut-off behavior at the blue end of the spectrum, is owing to the excitonic transition through direct electronic transitions from the valence band to the conduction band.

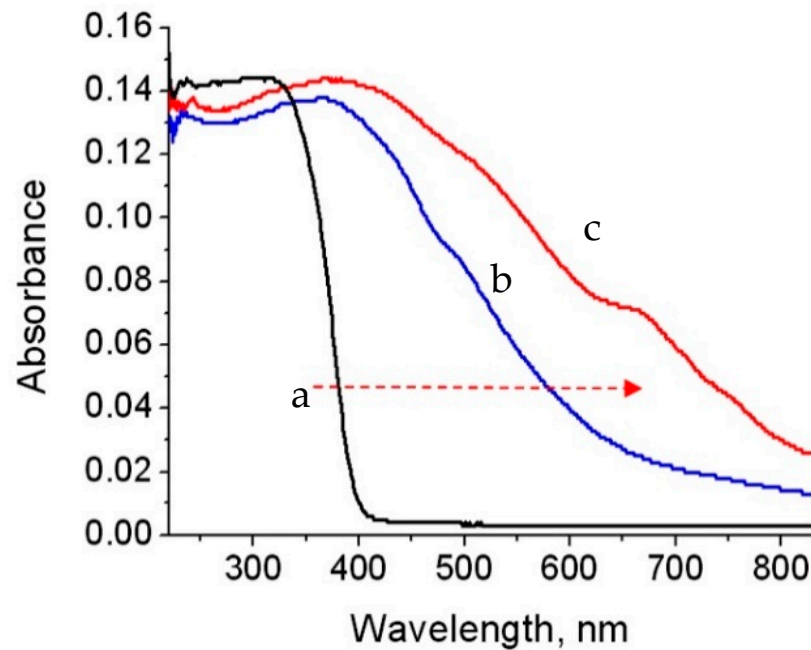


Figure 7. UV-Vis absorbance of: (a) BT nano commercial, (b) BT2-900 and (c) BT1-900.

Figure 7a displays the UV-Vis absorbance of the pure perovskite phase of BaTiO₃ nanoparticles. An absorption edge was observed at 400 nm with one maximum at 300 nm. By growing the hollandite phase, the absorption edge of the barium titanate perovskite phase was shifted to the visible region through the formation of mixed phases between perovskite and hollandite crystals to be sensitive in sunlight, as seen in Figure 7b. The absorption edge of BT2-900 was observed at 650 nm and its main absorption band was centered at 400 nm. This observation became clearer through preparing barium titanium oxides with only the hollandite phase, causing a red shift of barium titanate. Figure 7c shows that the absorption edge of the sample BT1-900 was observed at 800 nm, with two maxims at 430 nm and 650 nm. In addition, this red shift was further confirmed by calculating the energy band gap.

In order to calculate the energy band gap (E_g), the main absorption has been used according to the relation between the absorption coefficient (α) and the incident photon energy [41–44]:

$$(\alpha h\nu)^m = A(h\nu - E_g)$$

where the value (m) describes the optical absorption process and equals 2 or 1/2 for allowed direct and allowed indirect transitions, respectively, and A is constant. In the current materials, the value (m) is 2 because of the allowed direct transitions. Therefore, the optical band gap energy of the samples can be determined when $(\alpha h\nu)^2$ is zero. By plotting $(\alpha h\nu)^2$ and ($E = h\nu$), and extending the straight line to the (E) axis, as shown in Figure 8, the optical band gap of the samples becomes clear. Figure 8a shows that the band gap energy of barium titanium oxide nanoparticles with the perovskite phase is 3.2 eV.

By growing hollandite phases, the optical properties of barium titanium oxide nanoparticles are strongly modified through a reduction in band gap energy, as shown in Figure 8. In the case of BT2-900, the band gap energy decreased to 2.3 eV through growing the hollandite phase with the perovskite phase. This behavior continued through preparing barium titanium oxide nanoparticles with the hollandite phase only, as seen in the sample BT1-900. The band gap energy of BT1-900 was 2 eV. These results indicate that the narrowing of the band gap energy of the barium titanium oxide nanoparticles from 3.2 eV to 2.0 eV leads to the introduction of photocatalysts suitable to act and work in sunlight. This finding was confirmed by studying the optical behavior of the other samples, BT1-600 and BT2-600. Figure 9 reveals the absorbance spectrum of both BT1-600 and BT2-600 in the wavelength range of 200 to 800 nm. It means that these materials become active in

solar energy because of their broad absorbance in visible light. Figure 10 confirmed the improvement of optical properties through narrowing the band gap energy, indicating 1.75 eV and 2.3 eV for BT1-600 and BT2-600, respectively. Similar behavior was observed for the samples BT1 and BT2. Figure 11 revealed wide absorbance in the same wavelength range of 200 to 800 nm. The band gap energy for both samples was 2.2 eV and 2.4 eV, respectively, as shown in Figure 12.

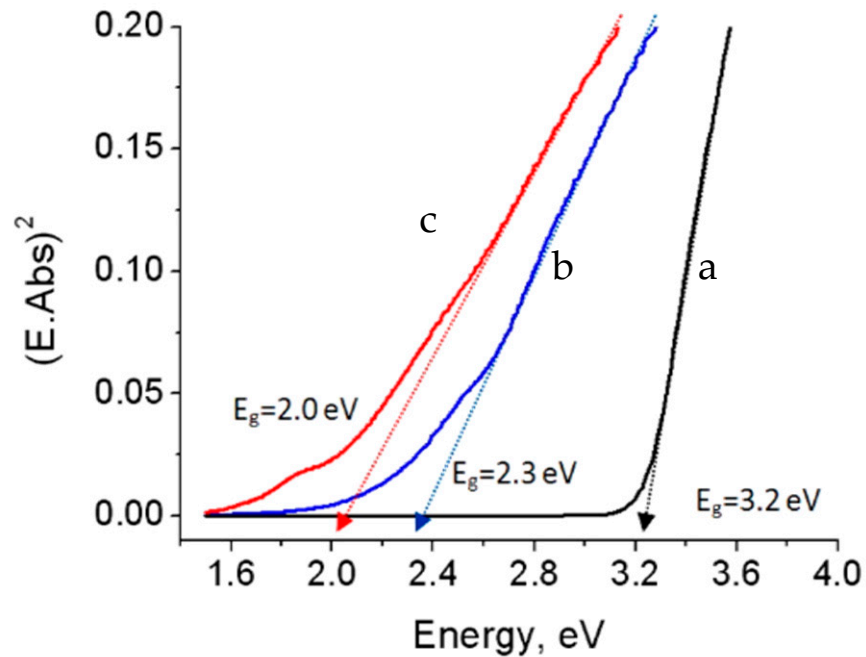


Figure 8. Band gap energy of: (a) BT nano commercial, (b) BT2-900 and (c) BT1-900.

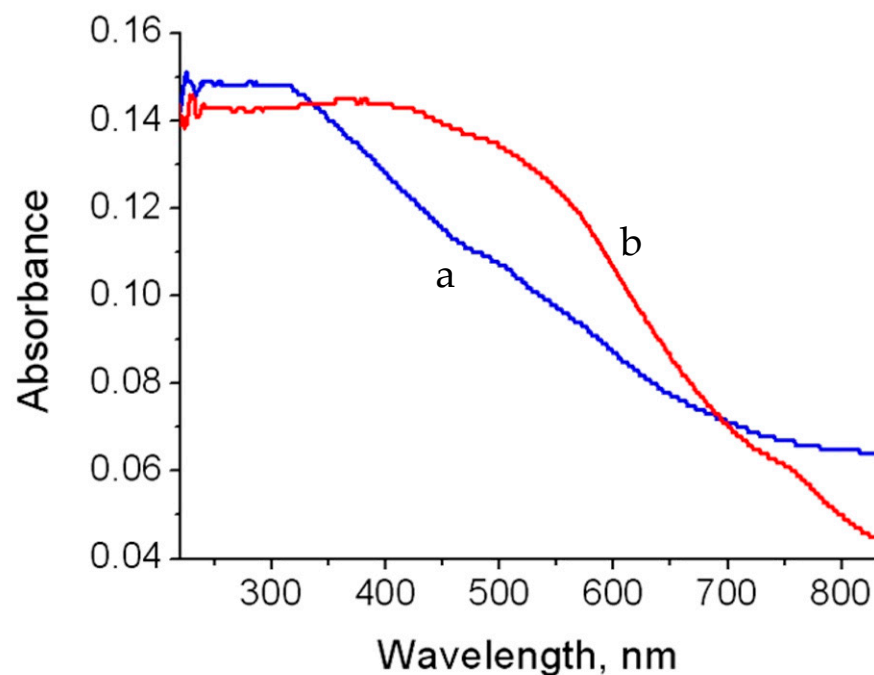


Figure 9. UV-Vis absorbance of: (a) BT2-600 and (b) BT1-600.

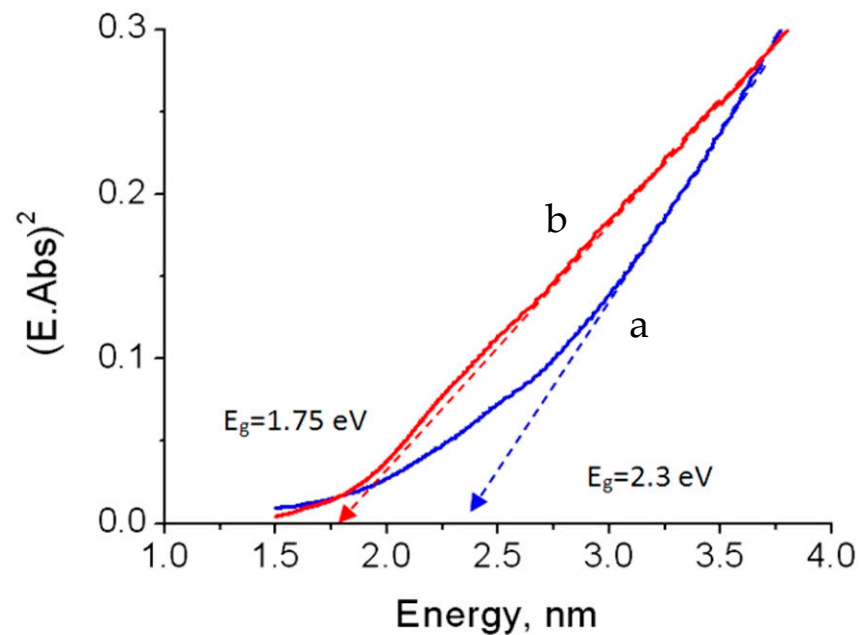


Figure 10. Band gap energy of: (a) BT2-600 and (b) BT1-600.

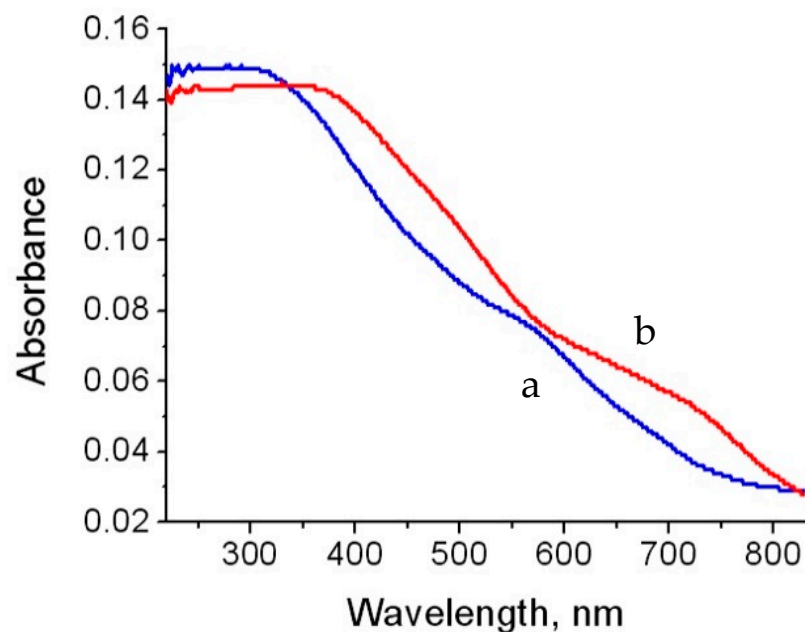


Figure 11. UV-Vis absorbance of: (a) BT2 and (b) BT1.

The solar activity of BT1-600, BT2-600, BT2-900 and BT1-900 was tested through photocatalytic degradation of the green dyes (naphthol green B; NGB) from water in the presence of sunlight.

At the same time, the commercial barium titanium oxide nanoparticles BaTiO_3 were used for comparison. The intensity of the absorption of naphthol green B at $\lambda_{\text{max}} = 720 \text{ nm}$ has been used for expressing the concentration of the green pollutants. High stability of NGB in sunlight was observed because there were no changes in the absorption of the green dye. The mixture between the green dye and one of the solid materials was irradiated for ten minutes in sunlight. After that, the absorbance of the green solution was measured and used as the concentration for the green dyes. These results are revealed in Figures 13 and 14. In the presence of BT1-900 or BT2-900, the absorbance of NGB was strongly reduced after irradiation for 10 min in sunlight, as seen in Figure 13. Figure 14

shows that BT1-900 and BT2-900 achieved 100% and 98% degradation of the pollutants, respectively. By using BT1-600 and BT2-600, the removal decreased to 91% and 84%, respectively, in the same period. This means that the complete removal and decolorization of the green pollutants were attained after using BT1-900. In the case of using the nanoparticles of barium titanium oxides with perovskite, a minor difference was observed for the absorbance of the pollutants after 10 min irradiation in sunlight, as revealed in Figure 13. Additionally, Figure 14 shows low performance for the perovskite phase because it caused 40% removal of the green dyes. This indicated that the perovskite phase is inactive in sunlight. In comparison with barium titanate having the perovskite phase, the samples containing the hollandite phase became very effective in the visible region. The presence of the hollandite phase caused broad absorbance and narrowing of the band gap energy to 2.0 eV, leading to complete removal of NGB in 10 min under sunlight.

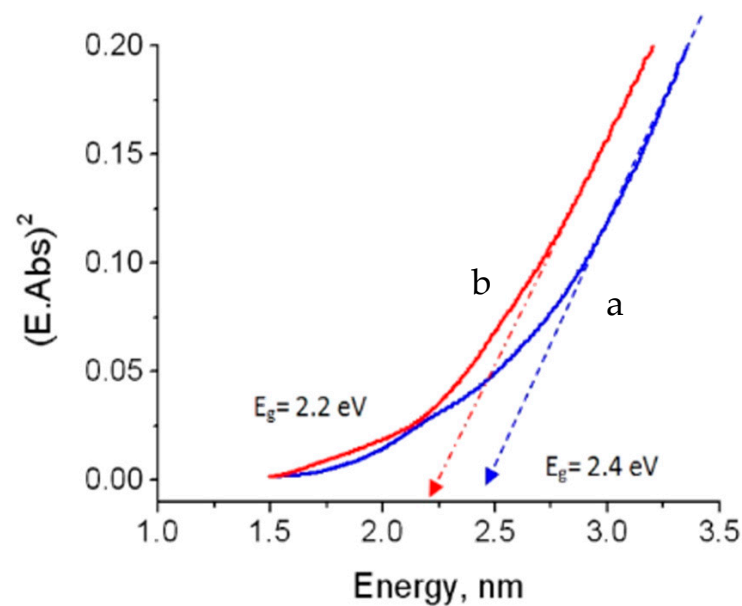


Figure 12. Band gap energy of: (a) BT2 and (b) BT1.

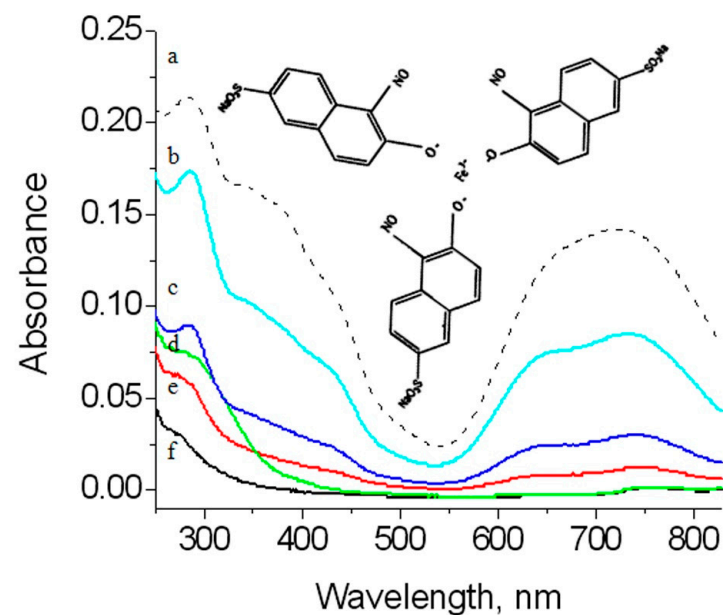


Figure 13. Absorbance spectra of naphthol green B after 10 min in sunlight (a) in the absence and in the presence of (b) BT nano commercial, (c) BT2-600, (d) BT2-900, (e) BT1-600 and (f) BT1-900.

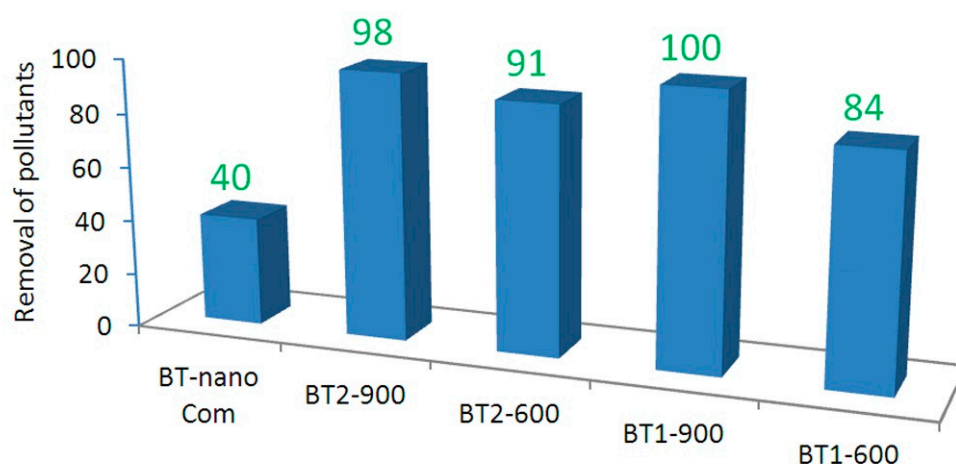


Figure 14. Percentage removal of naphthol green B after reacting for 10 min in sunlight.

4. Conclusions

In summary, BaTiO₃ with the hollandite phase was successfully prepared by the chemical route with heat treatment, using different temperatures to tune the phases of hollandites. X-ray diffracted patterns confirmed that the prepared product calcined at 900 °C was the hollandite type, which is well matched with standard data. However, the samples treated at 600 °C were found to be in mixed phases. In addition, with the increase in calcination temperature, the crystalline size of the barium hollandite was tuned. Raman spectra of the samples furthermore confirmed the formation of the hollandite phase in BaTiO₃ with characteristic peaks of hollandite structures. With an increase in calcination temperature, the peak intensity of Raman modes was found to be shifted. UV–Vis studies showed that the tuning of band gap could be accomplished by changing the calcination temperatures of BaTiO₃. The energy band gap was found to decrease from 3.2 eV to 2.0 eV and the samples showed a visible light response with enhanced optical properties. The photocatalytic capabilities of BaTiO₃ with hollandite phase were tested by means of UV–Vis absorption for the photo-degradation of green dye. The results showed that the samples having the hollandite phase became very effective in the visible region and degraded the green pollutant completely (100%) within 10 minutes. The obtained results have shown enhanced photocatalytic properties in visible light, which indicated that BaTiO₃ with hollandite phase is a suitable candidate for a novel photocatalyst for pollutant degradation.

Author Contributions: Conceptualization, A.A., O.S.; Data curation, O.S., F.A.; Formal analysis, F.A., O.S.; Funding acquisition, A.A.; Methodology, O.S., F.A.; Resources, A.A.; Visualization, A.A., F.A., O.S.; Writing—original draft, O.S., F.A.; Writing—review and editing, A.A., O.S., F.A. All authors have read and agreed to the published version of the manuscript.

Funding: This research was funded by Deanship of Scientific Research at King Faisal University for supporting this research through the Ra’ed track grant number 187010 and the APC was funded by [Ra’ed track].

Institutional Review Board Statement: Not Applicable.

Informed Consent Statement: Not Applicable.

Data Availability Statement: Data could be available on request.

Acknowledgments: The authors would like to thank the Deanship of Scientific Research at King Faisal University for supporting this research through the Ra’ed track (Grant # No. 187010).

Conflicts of Interest: The authors declare that they have no competing interests.

References

1. Fujishima, A.; Honda, K. Electrochemical Evidence for the Mechanism of the Primary Stage of Photosynthesis. *Bull. Chem. Soc. Jpn.* **1971**, *44*, 1148–1150. [[CrossRef](#)]
2. Fujishima, A.; Honda, K. Electrochemical Photolysis of Water at a Semiconductor Electrode. *Nat. Cell Biol.* **1972**, *238*, 37–38. [[CrossRef](#)] [[PubMed](#)]
3. Hardee, K.L.; Bard, A.J. Semiconductor Electrodes: I. The Chemical Vapor Deposition and Application of Polycrystalline N-Type Titanium Dioxide Electrodes to the Photosensitized Electrolysis of Water. *J. Electrochem. Soc.* **1975**, *122*, 739–742. [[CrossRef](#)]
4. Duonghong, D.; Borgarello, E.; Graetzel, M. Dynamics of light induced water cleavage in colloidal systems. *J. Am. Chem. Soc.* **1981**, *103*, 4685–4690. [[CrossRef](#)]
5. Kraeutler, B.; Bard, A.J. Heterogeneous photocatalytic decomposition of saturated carboxylic acids on TiO₂ powder—decarboxylative route to alkanes. *J. Am. Chem. Soc.* **1978**, *100*, 5985–5992. [[CrossRef](#)]
6. Asahi, R.; Morikawa, T.; Ohwaki, T.; Aoki, K.; Taga, Y. Visible-Light Photocatalysis in Nitrogen-Doped Titanium Oxides. *Science* **2001**, *293*, 269–271. [[CrossRef](#)]
7. Eliseev, A.A. Daylight Photocatalysis Achieved on Carbon-Doped TiO₂. *MRS Bull.* **2004**, *29*, 4–5. [[CrossRef](#)]
8. Adesina, A. Industrial exploitation of photocatalysis: Progress, perspectives and prospects. *Catal. Surv. Asia* **2004**, *8*, 265–273. [[CrossRef](#)]
9. Lee, W.W.; Chung, W.-H.; Huang, W.-S.; Lin, W.-C.; Lin, W.-Y.; Jiang, Y.-R.; Chen, C.-C. Photocatalytic activity and mechanism of nano-cubic barium titanate prepared by a hydrothermal method. *J. Taiwan Inst. Chem. Eng.* **2013**, *44*, 660–669. [[CrossRef](#)]
10. Mills, A.; Le Hunte, S. An overview of semiconductor photocatalysis. *J. Photochem. Photobiol. A Chem.* **1997**, *108*, 1–35. [[CrossRef](#)]
11. Peña, M.A.; Fierro, J.L.G. Chemical Structures and Performance of Perovskite Oxides. *Chem. Rev.* **2001**, *101*, 1981–2018. [[CrossRef](#)] [[PubMed](#)]
12. Adireddy, S.; Lin, C.; Cao, B.; Zhou, W.; Caruntu, G. Solution-Based Growth of Monodisperse Cube-Like BaTiO₃ Colloidal Nanocrystals. *Chem. Mater.* **2010**, *22*, 1946–1948. [[CrossRef](#)]
13. Cheary, R.W. An analysis of the structural characteristics of hollandite compounds. *Acta Crystallogr. Sect. B Struct. Sci.* **1986**, *42*, 229–236. [[CrossRef](#)]
14. Uheda, K.; Horiuchi, A.; Takizawa, H.; Endo, T. Synthesis and Crystal Structure of Novel Hollandite Compounds A_xMg_x/2Sn₈ – x/2O₁₆ (A = K, Rb, and Cs). *J. Porous Mater.* **1999**, *6*, 161–166. [[CrossRef](#)]
15. Aubin-Chevaldonnet, V.; Caurant, D.; Dannoux, A.; Gourier, D.; Charpentier, T.; Mazerolles, L.; Advocat, T. Preparation and characterization of (Ba,Cs)(M,Ti)₈O₁₆ (M = Al³⁺, Fe³⁺, Ga³⁺, Cr³⁺, Sc³⁺, Mg²⁺) hollandite ceramics developed for radioactive cesium immobilization. *J. Nucl. Mater.* **2007**, *366*, 137–160. [[CrossRef](#)]
16. Whittle, K.R.; Ashbrook, S.E.; Lumpkin, G.R.; Farnan, I.; Smith, R.I.; Redfern, S.A.T. The effect of caesium on barium hollandites studied by neutron diffraction and magic-angle spinning (MAS) nuclear magnetic resonance. *J. Mater. Sci.* **2007**, *42*, 9379–9391. [[CrossRef](#)]
17. Kesson, S.E.; White, T.J. [Ba_xCs_y][(Ti,Al)³⁺_{2x+y}Ti⁴⁺_{8–2x–y}]O₁₆ Synroc-Type Hollandites. I. Phase Chemistry. *Proc. R. Soc. Lond. Ser. A Math. Phys. Sci.* **1986**, *405*, 73–101.
18. Kesson, S.E.; White, T.J. [Ba_xCs_y][(Ti,Al)³⁺_{2x+y}Ti⁴⁺_{8–2x–y}]O₁₆ Synroc-Type Hollandites. II. Structural Chemistry. *Proc. R. Soc. Lond. Ser. A Math. Phys. Sci.* **1986**, *408*, 295–319.
19. Cheary, R.W. Structural Analysis of Hollandite Ba_xTi³⁺_{2x}Ti⁴⁺_{8–2x}O₁₆ with x = 1.07 and 1.31 from 5 to 500 K. *Acta Crystallogr.* **1990**, *46*, 599–609. [[CrossRef](#)]
20. Cheary, R.W. Caesium Substitution in the Titanate Hollandites Ba_xCs_y(Ti³⁺_{y+2x}Ti⁴⁺_{8–2x–y})O₁₆ from 5 to 400 K. *Acta Crystallogr.* **1991**, *47*, 325–333. [[CrossRef](#)]
21. Kesson, S.; White, T. Radius ratio tolerance factors and the stability of hollandites. *J. Solid State Chem.* **1986**, *63*, 122–125. [[CrossRef](#)]
22. Byström, A.M. The crystal structure of hollandite, the related manganese oxide minerals, and α-MnO₂. *Acta Crystallogr.* **1950**, *3*, 146–154. [[CrossRef](#)]
23. Watanabe, M.; Mori, T.; Yamauchi, S.; Yamamura, H. Catalytic property of the hollandite-type 1-D ion-conductors: Selective reduction of NO_x. *Solid State Ionics* **1995**, *79*, 376–381. [[CrossRef](#)]
24. Mori, T.; Yamauchi, S.; Yamamura, H.; Watanabe, M. New hollandite catalysis for the selective reduction of nitrogen monoxide with propene. *Appl. Catal. A* **1995**, *129*, L1–L7. [[CrossRef](#)]
25. Mori, T.; Yamauchi, S.; Yamamura, H.; Watanabe, M. KGa-priderite and related compound for the selective reduction of nitrogen monoxide with propylene. *J. Mater. Sci.* **1996**, *31*, 1469–1473. [[CrossRef](#)]
26. Mori, T.; Suzuki, J.; Fujimoto, K.; Watanabe, M. Photocatalysis decomposition of trichloro ethylene and nitrate ion in water on hollandite type catalysts. *J. Mater. Synth. Process.* **1998**, *6*, 329–333. [[CrossRef](#)]
27. Mori, T.; Suzuki, J.; Fujimoto, K.; Watanabe, M.; Hasegawa, Y. Reductive decomposition of nitrate ion to nitrogen in water on a unique hollandite photocatalyst. *Appl. Catal. B Environ.* **1999**, *23*, 283–289. [[CrossRef](#)]
28. Mori, T.; Suzuki, J.; Fujimoto, K.; Watanabe, M.; Hasegawa, Y. Photocatalytic Reduction of Nitrate in Water on Meso-Porous Hollandite Catalyst: A New Pathway on Removal of Nitrate in Water. *J. Sol-Gel Sci. Technol.* **2000**, *19*, 505–510. [[CrossRef](#)]
29. Suzuki, J.; Fujimoto, K.; Mori, T.; Watanabe, M.; Hasegawa, Y. Photocatalytic Reduction of NO with C₂H₆ on a Hollandite-Type Catalyst. *J. Sol-Gel Sci. Technol.* **2000**, *19*, 775–778. [[CrossRef](#)]

30. Filimonov, D.; Liu, Z.-K.; Randall, C. An oxygen nonstoichiometry study of barium polytitanates with hollandite structure. *Mater. Res. Bull.* **2002**, *37*, 2373–2382. [[CrossRef](#)]
31. Gao, W.L.; Deng, H.M.; Huang, D.J.; Yang, P.X.; Chu, J.H. Microstructure and optical properties of Zn-doped BaTiO₃ thin films. *J. Phys. Conf. Ser.* **2011**, *276*, 012163. [[CrossRef](#)]
32. Ohsaka, T.; Fujiki, Y. Raman spectra in hollandite type compounds K_{1.6}Mg_{0.8}Ti₁₆ and K_{1.6}A_{11.6}Ti_{6.4}O₁₆. *Solid State Commun.* **1982**, *44*, 1325–1327. [[CrossRef](#)]
33. Ohsaka, T.; Izumi, F.; Fujiki, Y. Raman Spectrum of anatase TiO₂. *J. Raman Spectrosc.* **1978**, *7*, 321–324. [[CrossRef](#)]
34. Shibata, Y.; Suemoto, T.; Ishigame, M. Raman scattering studies of mobile ions in superionic conductor hollandites. *Phys. Status solidi* **1986**, *134*, 71–79. [[CrossRef](#)]
35. Porto, S.P.S.; Fleury, P.A.; Damen, T.C. Raman Spectra of TiO₂, MgF₂, ZnF₂, FeF₂, and MnF₂. *Phys. Rev.* **1967**, *154*, 522–526. [[CrossRef](#)]
36. Tian, F.; Zhang, Y.; Zhang, J.; Pan, C. Raman Spectroscopy: A New Approach to Measure the Percentage of Anatase TiO₂ Exposed (001) Facets. *J. Phys. Chem. C* **2012**, *116*, 7515–7519. [[CrossRef](#)]
37. Roy, N.; Park, Y.; Sohn, Y.; Leung, K.T.; Pradhan, D. Green Synthesis of Anatase TiO₂ Nanocrystals with Diverse Shapes and their Exposed Facets-Dependent Photoredox Activity. *ACS Appl. Mater. Interfaces* **2014**, *6*, 16498–16507. [[CrossRef](#)]
38. Ishii, M.; Fujiki, Y.; Ohsaka, T. Raman scattering in one-dimensional ionic conductors Rb-priderites. *Solid State Commun.* **1985**, *55*, 1123–1126. [[CrossRef](#)]
39. Poyraz, A.S.; Huang, J.; Pelliccione, C.J.; Tong, X.; Cheng, S.; Wu, L.; Zhu, A.C.; Marschilok, K.J.; Takeuchi, E.S. Takeuchi. Synthesis of cryptomelane type a-MnO₂ (K_xMn₈O₁₆) cathode materials with tunable K⁺ Content: The role of tunnel cation concentration on electrochemistry. *J Mater Chem A* **2017**, *5*, 16914–16928. [[CrossRef](#)]
40. Knyazev, A.V.; Maćzka, M.; Ladenkov, I.V.; Bulanov, E.N.; Ptak, M. Crystal structure, spectroscopy, and thermal expansion of compounds in M¹₂O–Al₂O₃–TiO₂ system. *J Solid State Chem.* **2012**, *196*, 110–118. [[CrossRef](#)]
41. Maćka, P.; Pacia, M.; Macyk, W. How To Correctly Determine the Band Gap Energy of Modified Semiconductor Photocatalysts Based on UV–Vis Spectra. *J. Phys. Chem. Lett.* **2018**, *9*, 6814–6817. [[CrossRef](#)]
42. Viezbicke, B.D.; Patel, S.; Davis, B.E.; Birnie, D.P., III. Evaluation of the Tauc method for optical absorption edge determination: ZnO thin films as a model system. *Phys. Stat. Sol. B* **2015**, *252*, 1700–1710. [[CrossRef](#)]
43. Johannes, A.Z.; Pingak, R.K.; Bukit, M. Tauc Plot Software: Calculating energy gap values of organic materials based on Ultraviolet-Visible absorbance spectrum. *IOP Conf. Series Mater. Sci. Eng.* **2020**, *823*, 012030. [[CrossRef](#)]
44. Tauc, J.; Grigorovici, R.; Vancu, A. Optical Properties and Electronic Structure of Amorphous Germanium. *Phys. Status Solidi B* **1966**, *15*, 627–637. [[CrossRef](#)]